

Long Minority-Carrier Diffusion Length and Low Surface-Recombination Velocity in Inorganic Lead-Free CsSnI₃ Perovskite Crystal for Solar Cells

Bo Wu, Yuanyuan Zhou, Guichuan Xing, Qiang Xu, Hector F. Garces, Ankur Solanki, Teck Wee Goh, Nitin P. Padture,* and Tze Chien Sum*

Sn-based perovskites are promising Pb-free photovoltaic materials with an ideal 1.3 eV bandgap. However, to date, Sn-based thin film perovskite solar cells have yielded relatively low power conversion efficiencies (PCEs). This is traced to their poor photophysical properties (i.e., short diffusion lengths (<30 nm) and two orders of magnitude higher defect densities) than Pb-based systems. Herein, it is revealed that melt-synthesized cesium tin iodide (CsSnI₃) ingots containing high-quality large single crystal (SC) grains transcend these fundamental limitations. Through detailed optical spectroscopy, their inherently superior properties are uncovered, with bulk carrier lifetimes reaching 6.6 ns, doping concentrations of around $4.5 \times 10^{17} \text{ cm}^{-3}$, and minority-carrier diffusion lengths approaching 1 μm , as compared to their polycrystalline counterparts having $\approx 54 \text{ ps}$, $\approx 9.2 \times 10^{18} \text{ cm}^{-3}$, and $\approx 16 \text{ nm}$, respectively. CsSnI₃ SCs also exhibit very low surface recombination velocity of $\approx 2 \times 10^3 \text{ cm s}^{-1}$, similar to Pb-based perovskites. Importantly, these key parameters are comparable to high-performance p-type photovoltaic materials (e.g., InP crystals). The findings predict a PCE of $\approx 23\%$ for optimized CsSnI₃ SCs solar cells, highlighting their great potential.

skyrocketing to >20% within a few years of development.^[1–4] However, the presence of toxic Pb in PSCs has been a concern in the context of their widespread deployment in the future. In particular, hybrid perovskites are prone to decomposition, making the Pb susceptible to leaching into the environment. Thus, inorganic Pb-free (halide, chalcogenide, etc.) perovskites offer a viable solution to this challenge.^[5–9] Elements such as Sn, Bi, and Ge are less toxic, and they could potentially replace Pb in halide PSCs.^[6,10–15] Specifically, Sn-based perovskite CsSnI₃ (with bandgap $\approx 1.3 \text{ eV}$) is a promising candidate for PSCs, with its maximum Shockley–Queisser PCE limit of $\approx 33\%$.^[16,17] However, the state-of-the-art PCE of solution-processed CsSnI₃ polycrystalline (PC) PSCs without additives is merely 3%^[6,18]—far below PSCs based on Pb-containing perovskites. This deficiency is attributed to the high density of acceptor defects in

CsSnI₃, such as Sn or Cs vacancies (V_{Sn} or V_{Cs}), which have very low defect formation energies.^[19,20] This results in a material that is highly p-type, with heavily doped hole concentration as high as 10^{19} cm^{-3} . This is extremely detrimental to solar cell performance because efficient charge extraction and ambipolar charge transport are essential for high performance in PSCs.^[6,21]

The key to realizing the full potential of CsSnI₃ for solar cell applications is to develop strategies for reducing the defect density. Improving the crystalline quality through the synthesis, such as incorporation of additives (e.g., SnF₂),^[6] stoichiometry control,^[20] etc., is one approach. Alternatively, reduction in the number of grain boundaries—the source of high density of surface defects—could also have the same effect. This involves moving to very large-grained polycrystalline thin films or even SCs. In particular, it has been previously demonstrated that CsSnI₃ SCs can be fabricated using high-temperature reaction and melting of a stoichiometric mixture of CsI and SnI₂ in evacuated vials.^[19,22] The reduction of the grain boundaries, together with the high-temperature and vacuum-processed synthesis method, may yield high-quality CsSnI₃ with reduced defects for solar cell applications. Presently, the fundamental properties affecting the solar cell performance of SCs, e.g.,

1. Introduction

Perovskite solar cells (PSCs) based on Pb-containing hybrid organic–inorganic perovskites have attracted a great deal of attention, with their power conversion efficiencies (PCEs)

Dr. B. Wu, Dr. G. Xing, Dr. Q. Xu, A. Solanki,
T. W. Goh, Prof. T. C. Sum
Division of Physics and Applied Physics
School of Physical and Mathematical Sciences
Nanyang Technological University
21 Nanyang Link 637371, Singapore
E-mail: Tzechien@ntu.edu.sg

Dr. Y. Zhou, Dr. H. F. Garces, Prof. N. P. Padture
School of Engineering
Brown University
Providence, RI 02912, USA
E-mail: nitin_padture@brown.edu

Dr. G. Xing
Institute of Applied Physics and Materials Engineering
Faculty of Science and Technology
University of Macau
E12, Macao, SAR, China



DOI: 10.1002/adfm.201604818

doping concentrations, carrier lifetimes/diffusion lengths, surface-recombination velocities (SRVs), etc., are still unknown. Quantifying these properties and establishing a clear photo-physical picture of the SCs are paramount for the development of practical CsSnI₃ SC solar cells.

Here, ultrafast optical spectroscopy was used for the first time to investigate the photophysical properties of CsSnI₃ SCs. To preclude any degradation of CsSnI₃ in the air (i.e., Sn²⁺ oxidation to Sn⁴⁺) that could affect the intrinsic properties,^[23] all measurements were performed on melt-synthesized bulk ingots that were inside evacuated Pyrex vials in their as-fabricated condition. The slow-cooled ingots are expected to have single-crystal grains that are hundreds of microns in size, which is of the same order of the beam size used. Thus, all measurements reported here are essentially on CsSnI₃ SCs. The SCs show negligible erosion/degradation under repeated laser pulses with highly reproducible properties. Both transient emission and transient reflectance (TR) techniques reveal that the photoexcited carriers of the CsSnI₃ SCs possess very long bulk carrier lifetime of ≈ 6.6 ns, long minority carrier diffusion length of ≈ 930 nm, and a moderate intrinsic doping concentration of $\approx 4.5 \times 10^{17}$ cm⁻³. On the other hand, CsSnI₃ polycrystalline thin films (grain size ≈ 100 nm), formed either by solution processing or evaporation, exhibit carrier lifetime of ≈ 54 ps, minority-carrier diffusion length of ≈ 16 nm, and a doping concentration of $\gtrsim 9.2 \times 10^{18}$ cm⁻³, which is attributed to poor crystalline quality and increased grain boundaries. The

CsSnI₃ SCs also show negligible surface recombination velocity of $\lesssim 2 \times 10^3$ cm s⁻¹, implying that no further surface passivation (e.g., SnF₂ treatment) is needed. In addition, slow hot-carrier cooling of $\tau \approx 1$ ps in the CsSnI₃ SCs is comparable to Pb-based perovskites.^[24,25] Importantly, solar cell performance simulations using these parameters predict a PCE of around 23% in CsSnI₃ SCs solar cells.

2. Results

2.1. Basic Characterization and Properties

Figure 1a (inset) shows an as-synthesized CsSnI₃ ingot, which has a very smooth surface free of grain boundaries across a large area ($>10 \times 20$ μm^2), as seen in a scanning electron microscope (SEM) micrograph in Figure S1a (Supporting Information). At room temperature, the “black” CsSnI₃ perovskite exists in the orthorhombic crystal structure (space group *Pnma*).^[22] The X-ray diffraction (XRD) pattern of the crushed ingot powders was well-matched to the calculated XRD pattern (Figure S1b, Supporting Information) of orthorhombic CsSnI₃ perovskite. From UV photoelectron spectroscopy, it was found the valence band edge (VBM) is ≈ 4.72 eV below the vacuum level and the Fermi-level is only 0.16 eV above the VBM, confirming it is a p-type semiconductor (Figure S2, Supporting Information).

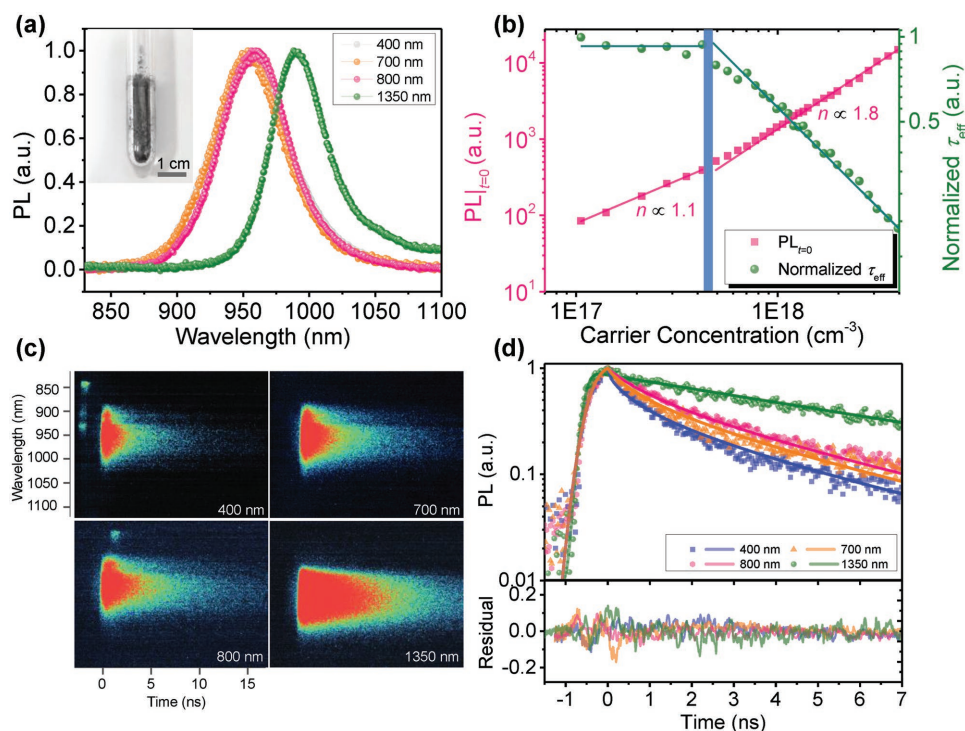


Figure 1. PL properties of CsSnI₃ SCs. a) PL spectra of CsSnI₃ with one-photon (400, 700, and 800 nm) and two-photon (1350 nm) excitations. Inset: Photograph of CsSnI₃ ingot inside an evacuated Pyrex vial. b) Carrier-concentration dependence of the effective PL lifetime (τ_{eff}) and intensity at $t = 0$ ($PL_{t=0}$). The green solid lines are guides for the eye. c) Pseudocolor images of TRPL profiles with one-photon and two-photon excitations. d) Top: PL dynamics with different photoexcitation energies. Solid lines are fits using the model described in the main text. The carrier densities were kept low ($<4 \times 10^{17}$ cm⁻³) to ensure that first-order recombination dominates. Bottom: fitting residuals.

2.2. Photoluminescence Properties

Figure 1a shows the CsSnI₃ SC photoluminescence (PL) spectra with one-photon (400, 700, and 800 nm) and two-photon (1350 nm) excitations. The PL spectra are centered at 950 nm (1.31 eV) with one-photon excitation, but redshift to 990 nm (1.25 eV) with two-photon excitation. This redshift can be attributed to PL re-absorption effect (e.g., high subgap absorption from tail states; small Stokes shift),^[26,27] and also to a smaller bandgap in the bulk crystal due to reduced lattice strain.^[28–30]

Figure 1b summarizes the carrier-concentration-dependent time-resolved PL (TRPL) data for CsSnI₃ SC. The PL intensity just after excitation ($t = 0$) can be used to evaluate the emission species in halide perovskite systems.^[31] Briefly, for emission dominated by free-carrier bimolecular recombination, the initial PL intensity exhibits a quadratic dependence with the photoexcited carrier concentration: $I_{\text{PL}}|_{t=0} \propto n_0^2$, where n_0 is the photoexcited carrier density; the effective carrier lifetime drops as intensity increases. For emission dominated by photoexcited carriers with doped carriers, the initial PL intensity exhibits a linear dependence with the photoexcited carrier concentration: $I_{\text{PL}}|_{t=0} \propto n_0 p_0$, where p_0 is the doped carrier concentration (or defect density); the effective carrier lifetime remains constant until all the doped carriers have recombined. It was found that the PL intensity following excitation increases linearly with carrier concentration in the low-density regime (carrier concentration $N_c < 4 \times 10^{17} \text{ cm}^{-3}$), whereas it has a nearly quadratic dependence in the high-density regime ($N_c > 5 \times 10^{17} \text{ cm}^{-3}$). Meanwhile, the effective PL lifetime also starts to drop under similar carrier concentrations. Such behavior corresponds to the recombination of excess minority carriers with unintentionally doped majority carriers or via mid-gap deep traps under weak excitation and bimolecular recombination of excess free carrier under intense excitation.^[31] In the CsSnI₃ system, the dominant point defect is V_{Sn} due to its low defect formation energy, which is a shallow native defect rendering CsSnI₃ an intrinsic p-type semiconductor.^[19] First-order recombination in the CsSnI₃ system occurs mainly in the case of excess electrons (minority carriers) recombining with the doped holes. Hence, from this we estimate an intrinsic doped hole concentration of $\approx 4\text{--}5 \times 10^{17} \text{ cm}^{-3}$, consistent with a previous report.^[19] Although some variations exist in samples from batch to batch, a general doping concentration of the order 10^{17} cm^{-3} can be consistently found for CsSnI₃ SCs. This value is higher than, or almost comparable to, that of the widely studied MAPbI₃ polycrystalline thin films (with typical values of $10^{15}\text{--}10^{17} \text{ cm}^{-3}$).^[31–33]

Comparative experiments were also performed on CsSnI₃ polycrystalline thin films sealed in vacuum. Their lifetimes start to decrease at a carrier concentration of $\approx 0.92 \times 10^{19} \text{ cm}^{-3}$. Simultaneously, the recombination order increases from first-order to higher order when Auger recombination and amplified stimulation emission occur. These results clearly show that the thin film is heavily doped by intrinsic defects. The defect density also agrees very well with previous reports (i.e., doped carrier concentration on the order of 10^{19} cm^{-3} (Figure S3, Supporting Information)).^[6,21] Generally, the thin films gave weak PL signal. Hence, we measured their PL from relatively brighter regions in an effort to obtain better signal-to-noise for the streak camera. This implies that the typical average

doped carrier concentration in these thin films should be $> 0.92 \times 10^{19} \text{ cm}^{-3}$. Such heavy intrinsic doping would greatly reduce the minority carrier mobilities and lifetimes, thus limiting the PSC performance.

To investigate the excitation-wavelength-dependent PL dynamics in CsSnI₃ SCs, we kept the photoexcited carrier concentrations to $< 4 \times 10^{17} \text{ cm}^{-3}$ to ensure dominant first-order recombination kinetics. Several wavelengths were chosen: 400, 700, and 800 nm for one-photon and 1350 nm for two-photon excitations. The pseudocolor images of the TRPL profiles are shown in Figure 1c, where a clear lifetime lengthening with increasing excitation wavelengths is evident. These decay transients at the $\approx 950 \text{ nm}$ emission were globally fitted (discussed later) as shown in Figure 1d. The PL decay using two-photon excitation shows a dominant single-exponential decay with a time constant of $6.6 \pm 0.1 \text{ ns}$. Given that two-photon excitation usually has a penetration depth on the order of $100 \mu\text{m}$,^[34] its PL decay lifetime can, therefore, be attributed to the bulk carrier lifetime. In contrast, the carrier lifetimes of solution-processed CsSnI₃ thin films range from 40 to 50 ps (i.e., from TRPL and transient absorption (TA)), which is two orders of magnitude lower than the bulk lifetimes from CsSnI₃ SCs (Figures S3 and S4, Supporting Information). To exclude any possible influence from effects such as inadvertent impurities incorporation from the solution-processing, we also prepared polycrystalline thin films by evaporating CsSnI₃ ingots in vacuum onto substrates. Consistently short lifetimes were also found for these evaporated thin films (Figure S5, Supporting Information). A direct conclusion is the greatly improved carrier lifetimes in CsSnI₃ SCs, which is attributed to the elimination of grain boundaries and surface defects. The high crystalline quality obtained using these high-temperature melting methods significantly reduced the intrinsic defects, which will be discussed in greater detail later. On the other hand, the dynamics of the CsSnI₃ SC PL emission from one-photon excitation is not only due to bulk carrier recombination but is also related to carrier diffusion and surface recombination, which accelerate the PL decay dynamics. As shown in Figure 1c, with highly absorbing excitation wavelengths (e.g., 400 nm), the effect from surface carrier diffusion and recombination is more severe than weakly absorbing excitation wavelengths (e.g., 800 nm). A model based on 1D diffusion was used to reproduce/simulate these processes^[35,36]

$$\frac{\partial N(x,t)}{\partial t} = D \frac{\partial^2 N(x,t)}{\partial x^2} - \frac{N(x,t)}{\tau} \quad (1)$$

where N is the carrier concentration, D is the diffusion coefficient, τ is the carrier lifetime, and x is the axis along the light propagation direction. Surface recombination occurs at the boundary with a velocity S

$$N(0,t) = \frac{D}{S} \left. \frac{\partial N(x,t)}{\partial x} \right|_{x=0}, \quad N(L,t) = 0$$

$$N(x,0) = N_0 \exp(-\alpha x).$$

where L is the thickness of the crystal, α is the excitation light absorption coefficient, and N_0 is the carrier concentration at $t = 0$ and $x = 0$. Applying the boundary conditions, the analytical solution of Equation (1) is

$$N(x, t) = \frac{N_0}{2} \exp\left(\frac{-t}{\tau_R}\right) \exp\left(-\frac{x^2}{4Dt}\right) \times \left[W\left(\alpha\sqrt{Dt} - \frac{x}{2\sqrt{Dt}}\right) - \frac{S + \alpha D}{S - \alpha D} W\left(\alpha\sqrt{Dt} + \frac{x}{2\sqrt{Dt}}\right) \right] + \frac{2S}{S - \alpha D} W\left(S\sqrt{\frac{t}{D}} + \frac{x}{2\sqrt{Dt}}\right) \quad (3)$$

where τ_R is the bulk carrier lifetime and $W(x) = \exp(x^2)\text{erfc}(x)$.

The collected PL from the crystal (after factoring over the 4π total solid angle) can be expressed as

$$I_{\text{PL}}(t) = A \int_0^L \int_0^{\theta_0} N(t, x) \exp\left(-\alpha_{\text{PL}} \frac{x}{\cos\theta}\right) 2\pi \sin\theta \, d\theta dx \quad (4)$$

where A is proportional to PL collection efficiency, α_{PL} is the absorption coefficient at the emission wavelength, L is the thickness of the SC, θ is the colatitude in spherical coordinates with zenith direction along the collection line direction, and θ_0 is the half apex angle of the light-emitting cone that can be collected by the lens. In our measurement θ_0 is $\approx 14^\circ$, resulting in a near-unity of the $\cos\theta$, hence the equation can be approximated to 1D. The collected PL dynamics depend on the carrier diffusion coefficient (D), surface recombination velocity (S), as well as the excitation/emission light absorption coefficients.

Different wavelength one-photon excitations alter the carrier distribution profiles as shown in Equation (3) due to the change in the absorption coefficients (α) and hence modify the PL dynamics in Equation (4). The diffusion coefficient (D) and surface recombination velocity (S) can be extracted by global-fitting the PL dynamics under different wavelength one-photon excitations. The global-fitting of the PL dynamics under three different excitation wavelengths (400, 700, and 800 nm) with distinct absorption coefficients ensures the fitted values of the shared parameters (D and S) are obtained with a high coefficient of determination (R -squared value: 0.9819). The fits revealed that D can be as large as $1.3 \pm 0.1 \text{ cm}^2 \text{ s}^{-1}$. Since the recombination ($\approx 10^{17} \text{ cm}^{-3}$) is mainly from photogenerated minority carriers with the doped carriers, the diffusion coefficient D is attributed to the minority carriers (electron), rendering a high minority-carrier mobility of $\approx 50 \text{ cm}^2 \text{ V}^{-1} \text{ s}^{-1}$ at room temperature. The high minority-carrier mobility, together with the long carrier lifetime, indicates that the minority carriers possess high diffusion capability. The contribution from surface recombination is rather small, with an SRV of $1.8 \pm 0.4 \times 10^3 \text{ cm s}^{-1}$. Such small SRV is comparable, or superior, to the best values reported for semiconducting crystals such as Ge,^[37] InP,^[38] MAPbBr₃,^[39] and MAPbI₃.^[34] The small contribution of the SRV to the carrier dynamics indicates that surface passivation is not necessary for CsSnI₃ SCs for solar cells or photodetector applications.

2.3. Transient Reflectance Spectroscopy

To further investigate the carrier dynamics and the nonradiative processes, we also performed TR spectroscopy (or TA under reflection geometry) on the CsSnI₃ SCs and correlated the

findings with the PL studies. Figure 2a,b shows pseudocolor TR profiles of CsSnI₃ SCs with 400 and 800 nm excitations. TR profiles with other excitation energies can be found in the Supporting Information (Figure S6, Supporting Information). The transient profiles in Figure 2c show typical antisymmetric peaks near the band edge, similar to previous reports for MAPbBr₃ and MAPbI₃ crystals.^[26,39] Halide perovskites have large refractive indices (i.e., $n \approx 3$ for CsSnI₃) in the visible to near infrared region (Figure S7, Supporting Information). Thus, the TR signal is dominated by the refractive index change (Δn) resulting from photoexcited state-filling.^[24,39] A detailed interpretation of the TR profile relies on the exact decomposition of the free carrier absorption, trap-state absorption, etc., which are still unknown. In our simple model, CsSnI₃ is treated as a direct bandgap semiconductor with near-band-edge absorption coefficient satisfying $\alpha \propto \sqrt{E - E_g}$, where E_g is the bandgap. The refractive index change (Δn) can be calculated using the Kramers–Kronig relations: $\Delta n(\omega) = \frac{c}{\pi} P \int_0^\infty \frac{\Delta\alpha(\omega')}{\omega'^2 - \omega^2} d\omega'$, where c

is the speed of light in vacuum, P is the Cauchy principal value of the integral, and $\Delta\alpha$ is the absorption coefficient change.^[40] We could satisfactorily reproduce the transient reflectance profile near the band edge (and up to $\approx 1050 \text{ nm}$) using $E_g \approx 1.33 \text{ eV}$ and the n - k data obtained from ellipsometry for a CsSnI₃ thin film (Figure S7, Supporting Information). The fitting results only start to deviate from the experimental results at around 1100 nm due to the presence of strong sub-bandgap states bleaching, which we did not take into account (Figure S6, Supporting Information). The isosbestic point between the two antisymmetric peaks basically reflects the average absorption position of the excited carriers; therefore, the dynamic change of the isosbestic point position corresponds to the energy position of the hot carriers. Before reaching a stable transient reflection profile at $\approx 10^2 \text{ ps}$, we observe a continuous redshift of the peaks and the isosbestic point within a few ps. This corresponds to the “hot-carrier” relaxation process in perovskite SCs.^[24,25] In addition, for high-energy photoexcitation (e.g., 400 and 500 nm pumping), a clear $+\Delta R$ region can be seen in the ultrafast time scale ($< 1 \text{ ps}$) just below the band edge (Figure 2a,d and Figure S6, Supporting Information). As shown in Figure 2d, the TR profile (with 400 nm excitation at 300 fs delay) at ultrashort timescale is completely different from the TR profiles at later delay times (Figure 2c). We attribute this behavior to arise from the interplay between the hot-carrier effects and the bandgap renormalization (BGR). Due to BGR after excitation, the bandgap is shifted to lower energy. High energy photoexcitation yields hot-carriers with high temperature, and as a result, the newly formed band edge due to BGR will be less occupied compared to the one at thermal equilibrium. This leads to the formation of a photoinduced absorption band below the bandgap that alters the shape of the TR profile.^[24] We find that the best fit of the TR profile at 300 fs with 400 nm excitation at a fluence of $\approx 2 \mu\text{J cm}^{-2}$ gave a carrier temperature of $\approx 1800 \text{ K}$ and a bandgap shift of $\Delta E = 0.1 \text{ eV}$.

After accounting for the spectral origins in TR spectra profiles, we next examine the TR kinetics. First, the rise time of the band-edge TR signal is important, as it corresponds to the relaxation of the hot-carriers to the band edge. As shown in Figure 2e, the rise time monitored at $\approx 920 \text{ nm}$ increases

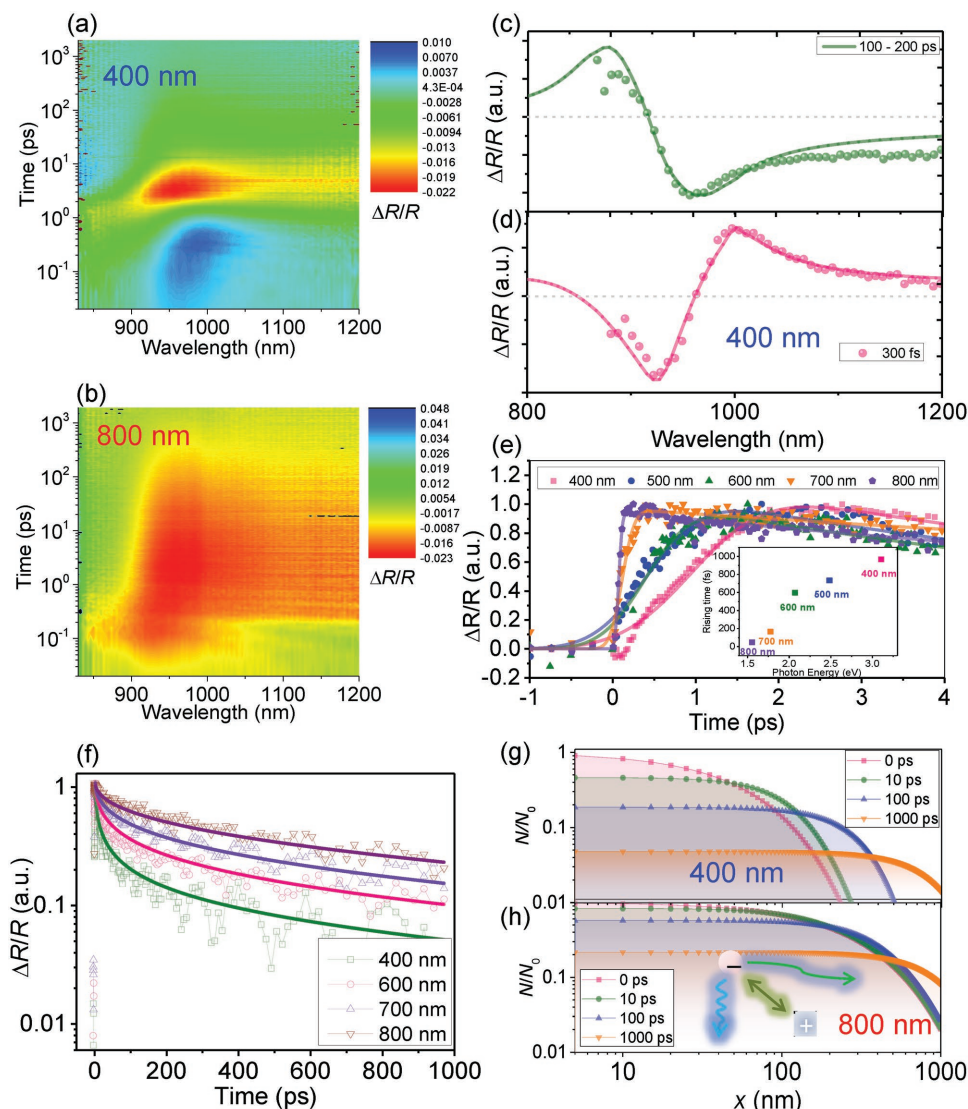


Figure 2. Transient reflection profiles and dynamics of CsSnI₃ SCs. The pseudocolor transient reflection profiles of CsSnI₃ SC with excitations: a) 400 nm and b) 800 nm. c) TR spectrum after most of the hot-carriers relaxed (i.e., few hundred ps). Both 400 and 800 nm excitations show the same TR spectrum profile. d) TR spectrum at early times (300 fs) when hot-carrier effect and BGR are both present with 400 nm excitation. e) The rising band-edge TR signal (monitored at 920 nm) following photoexcitation at various wavelengths. Inset: The fitted rise times at different photoexcitation energies. f) TR decay dynamics are found to accelerate with higher absorbing excitation photons, which can be fitted using a model based on surface recombination and diffusion. Simulated carrier distribution profiles with g) 400 nm and h) 800 nm excitations.

with higher energy photoexcitation. For example, with 400 nm high-energy photoexcitation, the rise time is ≈ 1 ps, indicating that the hot-carriers created by 400 nm excitation require ≈ 1 ps to relax to the band edge. Using $D = 1.3 \text{ cm}^2 \text{ s}^{-1}$, the hot carriers can diffuse as far as ≈ 11 nm before relaxation, which is close to the absorption length of 400 nm excitation light (≈ 50 nm). This also demonstrates the feasibility of harvesting hot-carriers from CsSnI₃ SCs.^[41,42]

The decay of the TR signal signifies the relaxation of carriers to the ground state. Due to the abrupt change of refractive index at the air (or glass)/perovskite interface, the TR signal is dominated by contributions from the surface region within a few nanometers.^[43,44] Hence, the carrier-induced reflectivity change could be evaluated by $N(0,t)$ in Equations (1)–(3)

$$N(t) = N_0 \exp\left(\frac{-t}{\tau_R}\right) \times \left[\frac{S}{S - \alpha D} W\left(S\sqrt{\frac{t}{D}}\right) - \frac{\alpha D}{S - \alpha D} W(\alpha\sqrt{Dt}) \right] \quad (5)$$

After the relaxation of hot-carriers, the dominating TR decay mechanism is carrier diffusion and surface/bulk recombination. The excitation intensity was set as low as possible (typically $\approx \mu\text{J cm}^{-2}$) to minimize any higher-order recombination. Negligible intensity dependence of the decay dynamics can be observed (Figure S8, Supporting Information) under the fluence regime we measured, indicating that the recombination is dominated by that between the minority carriers and the doped carriers. Hence, the measured diffusion is mainly from the minority carriers. This is

similar to the findings from PL emission dynamics where faster TR decay is observed when highly absorbing excitation photons are used. As shown in Figure 2f, global fitting of the TR decay data obtained from four different excitation wavelengths (400, 600, 700, and 800 nm) yielded a diffusion coefficient, D , of $1.9 \pm 0.1 \text{ cm}^2 \text{ s}^{-1}$, which is comparable to that determined from PL fittings. The contribution from surface recombination is also much smaller than that from diffusion, i.e., $S \ll \alpha D$, which makes it challenging to determine the exact value of the SRV. A high fitting uncertainty of $S = 0.8 \pm 1.2 \times 10^3 \text{ cm s}^{-1}$ was, therefore, obtained. Correlating with the earlier PL results, we believe that the acceptable value of the SRV in the CsSnI₃ SC is $< 2 \times 10^3 \text{ cm s}^{-1}$. The low SRV leads to a $\Delta R/R$ recovery that is dominated by carrier diffusion (the second term in the square brackets in Equation (5)), rather than surface recombination (the first term in the square brackets in Equation (5)). The simulated carrier distribution profiles after photoexcitation by 400 and 800 nm photons are shown in Figure 2g,h, respectively. The 400 nm excitation creates a high concentration of carriers in the shallower regions, which leads to more significant carrier diffusion compared to the 800 nm excitation.

3. Discussion

Carrier transport and recombination are greatly influenced by the intrinsic point defects (vacancies, interstitials and antisites), line defects (dislocation), surface defects (free surface and grain boundaries), etc.; SRV is, therefore, a very important parameter signifying the quality of an SC's surface and polycrystalline grain boundaries. Surface recombination is commonly attributed to the recombination from dangling bonds created deep surface defects and from impurities at the surface.^[45] Based on the Shockley–Read–Hall type recombination model, these defects/impurity levels should be most efficient in capturing both electrons and holes when they are located at the middle of the bandgap, resulting in the highest SRV. Low SRV semiconductors such as InP (10^2 cm s^{-1})²² and MAPbBr₃ (10^3 cm s^{-1})^[34,39] and high SRV semiconductors such as GaAs and CdTe ($>10^5 \text{ cm s}^{-1}$)^[46,47] are not only dependent on their crystal qualities but also on the position of their surface defect with respect to their energy bands. High crystalline quality indicates low defect densities in the bulk and at the surface—the latter determines the SRV. Using $S = \sigma v_{\text{th}} N_t$, where v_{th} is the carrier thermal velocity ($\approx 2 \times 10^7 \text{ cm s}^{-1}$), σ ($\approx 10^{-15} \text{ cm}^2$) is a typical recombination surface cross section in semiconductors, and N_t is surface trap density,^[48] we estimate a surface trap density of $< 10^{11} \text{ cm}^{-2}$, comparable to that of MAPbI₃ thin films ($\approx 5 \times 10^{11} \text{ cm}^{-2}$).^[49] In addition, we also performed density functional theory calculations on the electronic band structure of the bulk CsSnI₃ SC and the (001) surfaces. We found that the (001) surfaces terminated with either CsI or SnI will not introduce any surface states within the bandgap (Figure S9, Supporting Information), which may explain why the SRV in the high-quality CsSnI₃ single crystals can be so low ($< 2 \times 10^3 \text{ cm s}^{-1}$).

Carrier mobilities are determined by the average time between scattering processes. These processes include the

scattering by crystal defects/ionized impurities and by phonons. Carrier lifetime is greatly influenced by deep-level defects, which provide recombination centers. For intrinsically doped materials, the minority-carrier transport can be significantly impaired due to the presence of high amounts of donor or acceptor defects. This is undeniably the case for the CsSnI₃ polycrystalline thin films, where an intrinsic-doped carrier concentration as high as $0.92 \times 10^{19} \text{ cm}^{-3}$ was found. This high density of intrinsic defects renders it a heavily doped p-type material. The minority carrier diffusion length can be estimated by measuring PL quenching with an efficient electron extraction layer (e.g., PC₆₁BM), as described previously.^[50] Both methods of (i) depositing an efficient charge extraction layer to measure the carrier diffusion coefficient in thin films and (ii) using wavelength-dependent excitation to measure that in thick single crystals are well-established techniques based on a 1D diffusion model. The diffusion coefficients measured by both techniques are comparable, as shown for MAPbBr₃ single crystals,^[34,39] which are also comparable to the results using electrical techniques such as Hall effect and time-of-flight measurements.^[51,52] The PL lifetime drops slightly from 54.2 to 47.8 ps (Figure S10, Supporting Information). Assuming highly efficient electron extraction at the heterojunction, the decrease of PL lifetime corresponds to a minority-carrier mobility of $\approx 1.8 \text{ cm}^2 \text{ V}^{-1} \text{ s}^{-1}$ and a minority-carrier diffusion length of only $\approx 16 \text{ nm}$. The polycrystalline thin-film carrier-diffusion lengths are comparable to a previous report for another Sn-based hybrid perovskite (CH₃NH₃SnI₃, $\approx 30 \text{ nm}$ thickness), and it is responsible for the poor PSC performance obtained with polycrystalline thin films.^[11]

Unlike the polycrystalline case, the minority-carrier diffusion properties in CsSnI₃ SCs are greatly improved. Based on our above results, we estimate a diffusion length of the minority carriers (electrons) of around $930 \pm 70 \text{ nm}$ using $L = \sqrt{D\tau}$, where D is the diffusion coefficient and τ is the carrier lifetime. The minority carrier diffusion length is much higher than that of the absorption thickness (i.e., $\approx 300 \text{ nm}$ near the 900 nm band edge), and is comparable to that of the Pb-based perovskites.^[50,53] For more direct comparison with other p-type solar cells materials, Table 1 shows p-type InP with a similar direct bandgap (1.35 eV) possessing a diffusion coefficient of $5 \text{ cm}^2 \text{ s}^{-1}$, doping level of $4\text{--}5 \times 10^{16} \text{ cm}^{-3}$, lifetime of $\tau = 4 \text{ ns}$, and a comparable low SRV of 500 cm s^{-1} .^[38] Given that the best InP-based solar cells have a reported PCE of up to 22%,^[54,55] it is, therefore, entirely feasible to obtain high-PCE CsSnI₃ SCs-based solar cells.

Table 1. Comparison of key properties (i.e., bandgap, PL lifetime, minority carrier diffusion length, doped carrier concentration, and surface recombination velocity) that influence the PV performance for CsSnI₃ SC, PC, and p-type InP.

	E_g via PL [eV]	τ_{PL} [ns]	$L_{\text{minority carrier}}$ [nm]	n_{doped} [cm^{-3}]	SRV [cm s^{-1}]
CsSnI ₃ SC	1.31	6.6	930	4.5×10^{17}	$< 2 \times 10^3$
CsSnI ₃ PC	1.34	0.05	16	9.2×10^{18}	–
P-type InP	1.35 ^[38]	4 ^[38]	1400	5×10^{16} ^[38]	5×10^2 ^[38]

To correlate our findings to solar cell performance, we simulate the relation between surface recombination, grain size, and PCE. The PCEs are optimized values in which we assume the solar cells have optimized energy level alignments, Ohmic contacts, and efficient charge extraction by electrodes. Detailed procedures are elaborated on in the Experimental Section and the Supporting Information. The effective carrier lifetime is determined by the grain size (d), diffusion coefficient (D), and surface recombination velocity (S)^[39,56]

$$\frac{1}{\tau_{\text{eff}}} = \frac{1}{\tau_{\text{B}}} + \frac{1}{\frac{d}{2S} + \frac{1}{D} \left(\frac{d}{\pi} \right)^2} \quad (6)$$

In the equation, we assumed that the crystalline quality is not varying with grain size and that the grain boundaries in the polycrystalline films are the same as that of our single crystal surface, i.e., possessing the same concentration of recombination centers per unit area and capture cross sections, etc. The grain-size-dependent effective carrier lifetimes with selected SRVs (10^2 , 10^3 , 10^4 , 10^5 cm s^{-1}) are shown in Figure 3a. Upon shrinking the size of the grains from SC to small dimensions, there is a drastic drop in the lifetimes. Nonetheless, using the τ_{B} and S values obtained experimentally from our melt-synthesized CsSnI_3 SCs, we determined an effective lifetime of ≈ 3 ns for 300 nm size grains, which is much longer than the measured value of around 50 ps. This indicates that the crystallinity of the polycrystalline thin films is much worse than that of SC, resulting in much higher S at the grain boundaries and

lower bulk lifetime τ_{B} ; this deviation from the effective lifetime trend is obtained from Equation (6). Even for the evaporated thin films, the crystalline quality of the single crystal is not preserved during the evaporation process. Another possible reason is the grain boundaries of polycrystalline CsSnI_3 cannot be treated equivalent to that of the single crystal surface: the former provides much more deep defects (resulting from disorder/misorientation, unintentional impurities incorporation, fast degradation, stoichiometry deviations, etc.) that accelerate the grain-boundary recombination. Previously, we found that for solution-processed CsSnI_3 polycrystalline thin films, the emission lifetime increases from ≈ 70 ps without any additives to ≈ 1.4 ns with SnF_2 additive.^[57] In that earlier study, it was suggested that the SnF_2 addition optimized the crystallization process and reduced the defect density.

To gain deeper insights into the relations between grain size, SRV, and PSC performance, we fixed the bulk carrier lifetime value obtained from SC (≈ 6 ns), and plotted a pseudocolor map of the PCE with varying grain sizes and SRV as shown in Figure 3b. Theoretically, 23% PCE can be obtained using CsSnI_3 SCs or large-grained polycrystalline thin films under optimized conditions. The size-dependent PCE, short-circuit current density (J_{SC}), fill factor (FF), and open-circuit voltage (V_{OC}) using the bulk lifetime and SRV from SCs are shown in Figure 3c. For comparison, we also presented the performance with non-optimized parameters from polycrystalline CsSnI_3 without SnF_2 addition. We first assumed that $1/\tau_{\text{B}}$ and S scale by the same factor when translating from optimized SC fabrication conditions (with higher crystalline quality) to the nonoptimized

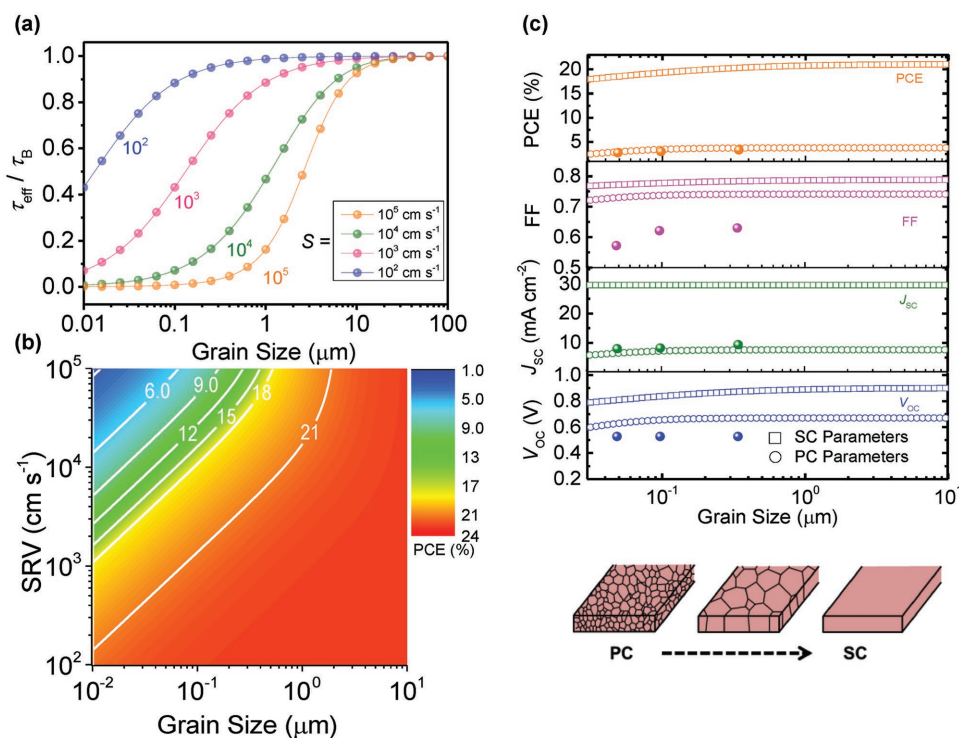


Figure 3. a) Dependence of the effective carrier lifetime on the grain size and SRV. b) Pseudocolor simulated PCE and its dependence on SRV and grain size. c) Prediction of solar cell performance parameters (V_{OC} , J_{SC} , FF, and PCE) as a function of grain size using parameters from SCs (thickness: 300 nm) and PCs (thickness: 100 nm). The thicknesses are almost optimized for both cases. Solid circles are experimental data obtained for solar cells based on CsSnI_3 polycrystalline thin films without any additives.^[5]

thin-film fabrication conditions (with poorer crystalline quality) (i.e., increased defect density both at the grain boundary and in the bulk crystal). The scaling factor is around 10^2 (calculated using Equation (6)), which is consistent with the approximately two orders of magnitude increase in defect density in SC compared to polycrystalline thin film. The simulated device performance with these increased S and $1/\tau_B$ is shown in Figure 3c, which is consistent with our recent experimental results (solid circles).^[5] The simulated V_{OC} and FF are higher than the experimental results, as the simulation is based on ideal and optimized conditions. The grain-size-dependent J_{SC} is slightly lower than the reported value, possibly due to a passivation of the defects at the interfaces by the charge transport layers in a real device. Hence, replacement of polycrystalline thin films with the high-temperature-synthesized SCs would allow larger improvements to the performance of CsSnI₃-based PSCs. It is important to note that the predicted 23% PCE need not be the ultimate upper limit for CsSnI₃ SCs. Usually, moderate doping concentration and high-quality materials (with as few as possible deep-level defects) are needed to obtain maximum device efficiency, e.g., in Si-based solar cells, the optimized carrier concentration is $\approx 10^{16}$ cm⁻³.^[58] The intrinsic doping concentration and deep-level defects formation in CsSnI₃ SCs can be further optimized with judicious chemical tuning (e.g., adding SnF₂, modifying stoichiometry, optimizing synthesis methods, etc.) or physical tuning (e.g., ion implantation, ion diffusion, annealing, etc.) of the doping concentration. Currently, fabricating solar cells using these CsSnI₃ ingots is still very challenging: the critical step is to precisely control the thickness of the single crystals to be comparable to the carrier diffusion length (≈ 1 μm). This requires new technique developments in perovskite single crystal slicing, polishing, as well as other growing methods typical for monocrystalline inorganic semiconductors (e.g., molecular beam epitaxy). We anticipate a great leap in performance once the new methods fabricating high-quality and thin CsSnI₃ single crystals are developed. Furthermore, the stability of CsSnI₃ SCs is still far from satisfactory. Under ambient conditions (20 °C, 60% humidity, continuous illumination), the PL was quenched within 2 h (Figure S11, Supporting Information). Comparatively, the stability is better for SCs than thin films. Nonetheless, we envisage that such stability issues will be gradually mitigated as the field progresses, just like in the case of MAPbI₃.

4. Conclusion

Using ultrafast optical spectroscopies, we uncovered that melt-synthesized CsSnI₃ ingots have exceptional photophysical properties as active layer material for PV application. The minority carriers possess a diffusion length approaching 1 μm, which is much longer than the absorption length and greatly improved compared to polycrystalline thin films of around 16 nm. We interpret these as a consequence of reduced grain boundaries and improved crystalline quality that lead to much lower defect densities, higher minority carrier mobility, and lifetime. The SRV is very low ($< 2 \times 10^3$ cm s⁻¹) contributing negligibly to the photophysical dynamics, which indicates the ingots do not need any surface passivation to achieve optimal performance. Thus, these findings suggest that replacing polycrystalline thin

films with melt-synthesized ingots is expected to provide a performance leap for CsSnI₃-based solar cells.

5. Experimental Section

Crystal Synthesis and Characterization: The synthesis of CsSnI₃ perovskite ingot-containing large single crystal grains follows a similar procedure that is reported elsewhere.^[13,57] Stoichiometric amounts of SnI₂ (Alfa, USA) and CsI (Sigma-Aldrich, USA) were mixed and placed in pyrex vials (≈ 3 mm diameter). The vials were then evacuated to 5×10^{-6} Torr vacuum for 9 h and sealed using a oxy-methane torch. The evacuated vials were then placed in a tube furnace and heated to 550 °C (above the melting point of CsSnI₃ perovskite of 435 °C) and held for 26 min, followed by slow cooling at a rate of 0.04 °C min⁻¹ to room temperature. For SEM (LEO 1530VP, Carl Zeiss, Munich, Germany) observation, the vial was broken and the CsSnI₃ ingot sample was quickly transferred to the SEM chamber and evacuated. For XRD characterization, the vial was broken inside an N₂-filled glove box, and the ingot was crushed into a powder. The powder was spread onto a holder and loaded in an X-ray transparent chamber. The sample was removed from the glove box and XRD (Bruker D8-advance, Karlsruhe, Germany) was performed using Cu K_α radiation and the following parameters: 2θ range 10° to 60°, 0.02° step scan. The resulting XRD pattern was indexed with the help of the PDF2 database. The stimulated XRD experiment is performed using the PowderCell 2.3 software based on a stoichiometric CsSnI₃ orthorhombic crystal model; instrumental broadening is considered in this model. The polycrystalline thin films of CsSnI₃ perovskite were deposited using two different methods—solution processing and evaporation—on glass substrates inside an N₂-filled glove box or under high-vacuum condition (10⁻⁵ Pa). The films were then sealed before removing them into the ambient for further characterization.

TIPL and TRPL: Time-integrated photoluminescence (TIPL) measurements were conducted by directing the excitation laser pulses onto the ingots/thin films. The PL was collected at a backscattering angle by a spectrometer (Acton, Spectra Pro 2500i) and Charge-coupled device (CCD, Princeton Instruments, Pixis 400B). Time-resolved photoluminescence (TRPL) was collected using an Optronis Optoscope streak camera system that has an ultimate temporal resolution of 6 ps.

TR Spectroscopy: Transient reflection (TR) measurements were performed using a commercial nondegenerate Helios (Ultrafast Systems LLC) pump-probe setup in reflection geometry. Both the pump and probe beams have a very small incident angle ($< 10^\circ$) in the TR measurement. The pump pulses were generated from an optical parametric amplifier (Light Conversion TOPAS) that was pumped by a 1 kHz regenerative amplifier (Coherent Legend, 800 nm, 150 fs, 1 mJ). A mode-locked Ti-sapphire oscillator (Coherent Vitesse, 80 MHz) was used to seed the amplifier. The probe pulses were a white light continuum generated by passing the 800 nm fs pulses through either a 2 mm sapphire plate for visible part (400–800 nm) or a 1 cm sapphire plate for NIR part (800–1600 nm). The probe light was collected using a CMOS sensor for UV–vis part and InGaAs diode array sensor for NIR part. To improve the signal-to-noise ratio, the same sensor was used to collect the probe light before the sample as a reference.

Device Simulation: The short-circuit current density (J_{SC}), open-circuit voltage (V_{OC}), and FF determine the output power-conversion efficiency: $PCE = (J_{SC} \times V_{OC} \times FF) / P_{in}$, where P_{in} is the input power ($= 100$ mW cm⁻² for “one-sun” conditions). The optimized device performance was simulated. Part of the simulation was performed in a similar manner to that in a previous report as illustrated below.^[59] The V_{OC} can be expressed as^[60]

$$V_{OC} = \frac{nkT}{q} \ln \left(\frac{J_{SC}}{J_0} \right) \quad (7)$$

where n is the ideal factor determined by the recombination type, kT/q is the thermal energy, and J_0 is the reverse saturation current density in the dark. The dark current is expressed as

$$J_d = J_{od} \exp(\lambda_d V) + J_{or} \exp(\lambda_r V) \quad (8)$$

where $\lambda_d = q/kT$, $\lambda_r = q/2kT$. $J_{od} = qD_p p_{n0}/L_p + qD_n n_{p0}/L_n$ is the diffusion-induced reverse saturation current density and $J_{od} = qn_i W/2\tau_{eff}$ is the recombination-induced reverse saturation current density. $D_{p,n}$ and $L_{p,n}$ are the diffusion coefficients and diffusion lengths for holes and electrons, respectively. W is the depletion width of ≈ 50 nm using the effective mass of electrons and holes of $0.16 m_0$ and $0.07 m_0$, respectively.^[23] It is found that the latter contribution dominates for CsSnI₃ in our case. For optimized solar cell, the FF is related to the V_{OC} ^[61]

$$FF = \frac{\frac{V_{OC}}{nkT/q} - \ln\left(\frac{V_{OC}}{nkT/q} + 0.72\right)}{\frac{V_{OC}}{nkT/q} + 1} \quad (9)$$

For J_{SC} , it was previously treated as a constant assuming that the strong built-in field can extract all the photogenerated charges under short-circuit condition for optimized MAPbI₃ devices. However, for CsSnI₃, the diffusion lengths under poorer working conditions do not necessarily result in the extraction of all the charges. Hence, $J_{SC} = J_{drift} + J_{diffuse}$ was used to calculate the charge extraction efficiency, where the first term on the right side accounts for the current originating from minority carrier drift in the depletion region and the second term accounts for carrier diffusion out of the depletion region. For good working conditions such as shown in the main text for vacuum-processed single crystals, the J_{SC} is approximately a constant, while using parameters from polycrystalline thin films without additives, the J_{SC} varies significantly for small grain size. Further details of the calculations are provided in the Supporting Information.

Supporting Information

Supporting Information is available from the Wiley Online Library or from the author.

Acknowledgements

B.W. and Y.Z. contributed equally to this work. The work received financial support from Nanyang Technological University start-up grant M4080514; the Ministry of Education Academic Research Fund Tier 1 grant RG101/15, and Tier 2 grants MOE2014-T2-1-044 and MOE2015-T2-2-015; and from the Singapore National Research Foundation through the Singapore–Berkeley Research Initiative for Sustainable Energy (SinBeRISE) CREATE Program, and the Competitive Research Program NRF-CRP14-2014-03 is gratefully acknowledged. Y. Zhou, H.F. Garces, and N.P. Padture are grateful to the US National Science Foundation (Award Nos. DMR-1305913 and OIA-1538893) for the financial support.

Received: September 16, 2016

Revised: October 31, 2016

Published online: January 5, 2017

- [1] A. Kojima, K. Teshima, Y. Shirai, T. Miyasaka, *J. Am. Chem. Soc.* **2009**, *131*, 6050.
- [2] H.-S. Kim, C.-R. Lee, J.-H. Im, K.-B. Lee, T. Moehl, A. Marchioro, S.-J. Moon, R. Humphry-Baker, J.-H. Yum, J. E. Moser, M. Graetzel, N.-G. Park, *Sci. Rep.* **2012**, *2*, 591.
- [3] M. M. Lee, J. Teuscher, T. Miyasaka, T. N. Murakami, H. J. Snaith, *Science* **2012**, *338*, 643.
- [4] W. S. Yang, J. H. Noh, N. J. Jeon, Y. C. Kim, S. Ryu, J. Seo, S. I. Seok, *Science* **2015**, *348*, 1234.
- [5] N. Wang, Y. Zhou, M. Ju, H. F. Garces, T. Ding, S. Pang, X. C. Zeng, N. P. Padture, X. W. Sun, *Adv. Energy Mater.* **2016**, *6*, 1601130.
- [6] M. H. Kumar, S. Dharani, W. L. Leong, P. P. Boix, R. R. Prabhakar, T. Baikie, C. Shi, H. Ding, R. Ramesh, M. Asta, M. Graetzel, S. G. Mhaisalkar, N. Mathews, *Adv. Mater.* **2014**, *26*, 7122.
- [7] W. W. Meng, B. Saparov, F. Hong, J. B. Wang, D. B. Mitzi, Y. F. Yan, *Chem. Mater.* **2016**, *28*, 821.
- [8] Y. Y. Sun, M. L. Agiorgousis, P. H. Zhang, S. B. Zhang, *Nano Lett.* **2015**, *15*, 581.
- [9] S. Perera, H. L. Hui, C. Zhao, H. T. Xue, F. Sun, C. H. Deng, N. Gross, C. Milleville, X. H. Xu, D. F. Watson, B. Weinstein, Y. Y. Sun, S. B. Zhang, H. Zeng, *Nano Energy* **2016**, *22*, 129.
- [10] F. Hao, C. C. Stoumpos, D. H. Cao, R. P. H. Chang, M. G. Kanatzidis, *Nat. Photonics* **2014**, *8*, 489.
- [11] N. K. Noel, S. D. Stranks, A. Abate, C. Wehrenfennig, S. Guarnera, A. A. Haghighirad, A. Sadhanala, G. E. Eperon, S. K. Pathak, M. B. Johnston, A. Petrozza, L. M. Herz, H. J. Snaith, *Energy Environ. Sci.* **2014**, *7*, 3061.
- [12] B. W. Park, B. Philippe, X. L. Zhang, H. Rensmo, G. Boschloo, E. M. J. Johansson, *Adv. Mater.* **2015**, *27*, 6806.
- [13] T. Krishnamoorthy, H. Ding, C. Yan, W. L. Leong, T. Baikie, Z. Y. Zhang, M. Sherburne, S. Li, M. Asta, N. Mathews, S. G. Mhaisalkar, *J. Mater. Chem. A* **2015**, *3*, 23829.
- [14] P. P. Sun, Q. S. Li, L. N. Yang, Z. S. Li, *Nanoscale* **2016**, *8*, 1503.
- [15] P. P. Sun, Q. S. Li, S. Feng, Z. S. Li, *Phys. Chem. Chem. Phys.* **2016**, *18*, 14408.
- [16] W. Shockley, H. J. Queisser, *J. Appl. Phys.* **1961**, *32*, 510.
- [17] S. Ruhle, *Sol. Energy* **2016**, *130*, 139.
- [18] Z. Chen, J. J. Wang, Y. Ren, C. Yu, K. Shum, *Appl. Phys. Lett.* **2012**, *101*, 093901.
- [19] I. Chung, J. H. Song, J. Im, J. Androulakis, C. D. Malliakas, H. Li, A. J. Freeman, J. T. Kenney, M. G. Kanatzidis, *J. Am. Chem. Soc.* **2012**, *134*, 8579.
- [20] P. Xu, S. Y. Chen, H. J. Xiang, X. G. Gong, S. H. Wei, *Chem. Mater.* **2014**, *26*, 6068.
- [21] J. Zhang, C. H. Yu, L. L. Wang, Y. Z. Li, Y. H. Ren, K. Shum, *Sci. Rep.* **2014**, *4*, 6954.
- [22] I. Chung, B. Lee, J. Q. He, R. P. H. Chang, M. G. Kanatzidis, *Nature* **2012**, *485*, 486.
- [23] W. J. Yin, J. H. Yang, J. Kang, Y. F. Yan, S. H. Wei, *J. Mater. Chem. A* **2015**, *3*, 8926.
- [24] M. B. Price, J. Butkus, T. C. Jellicoe, A. Sadhanala, A. Briane, J. E. Halpert, K. Broch, J. M. Hodgkiss, R. H. Friend, F. Deschler, *Nat. Commun.* **2015**, *6*, 8420.
- [25] Y. Yang, D. P. Ostrowski, R. M. France, K. Zhu, J. van de Lagemaat, J. M. Luther, M. C. Beard, *Nat. Photonics* **2016**, *10*, 53.
- [26] Y. Yamada, T. Yamada, L. Q. Phueng, N. Maruyama, H. Nishimura, A. Wakamiya, Y. Murata, Y. Kanemitsu, *J. Am. Chem. Soc.* **2015**, *137*, 10456.
- [27] H. Wang, K. S. Wong, B. A. Foreman, Z. Y. Yang, G. K. L. Wong, *J. Appl. Phys.* **1998**, *83*, 4773.
- [28] W. Y. Nie, H. H. Tsai, R. Asadpour, J. C. Blancon, A. J. Neukirch, G. Gupta, J. J. Crochet, M. Chhowalla, S. Tretiak, M. A. Alam, H. L. Wang, A. D. Mohite, *Science* **2015**, *347*, 522.
- [29] V. D'Innocenzo, A. R. S. Kandada, M. De Bastiani, M. Gandini, A. Petrozza, *J. Am. Chem. Soc.* **2014**, *136*, 17730.
- [30] G. Grancini, S. Marras, M. Prato, C. Giannini, C. Quarti, F. De Angelis, M. De Bastiani, G. E. Eperon, H. J. Snaith, L. Manna, A. Petrozza, *J. Phys. Chem. Lett.* **2014**, *5*, 3836.
- [31] Y. Yamada, T. Nakamura, M. Endo, A. Wakamiya, Y. Kanemitsu, *J. Am. Chem. Soc.* **2014**, *136*, 11610.
- [32] G. C. Xing, N. Mathews, S. S. Lim, N. Yantara, X. F. Liu, D. Sabba, M. Graetzel, S. Mhaisalkar, T. C. Sum, *Nat. Mater.* **2014**, *13*, 476.
- [33] S. D. Stranks, V. M. Burlakov, T. Leijtens, J. M. Ball, A. Goriely, H. J. Snaith, *Phys. Rev. Appl.* **2014**, *2*, 034007.

- [34] B. Wu, H. T. Nguyen, Z. Ku, G. Han, D. Giovanni, N. Mathews, H. J. Fan, T. C. Sum, *Adv. Energy Mater.* **2016**, *6*, 1600551.
- [35] J. Vaitkus, *Phys. Status Solidi A: Appl. Res.* **1976**, *34*, 769.
- [36] C. A. Hoffman, K. Jarasiunas, H. J. Gerritsen, A. V. Nurmikko, *Appl. Phys. Lett.* **1978**, *33*, 536.
- [37] N. Derhacopian, P. Fine, J. T. Walton, Y. K. Wong, C. S. Rossington, P. N. Luke, *IEEE Trans. Nucl. Sci.* **1994**, *41*, 1026.
- [38] Y. Rosenwaks, Y. Shapira, D. Huppert, *Phys. Rev. B* **1992**, *45*, 9108.
- [39] Y. Yang, Y. Yan, M. J. Yang, S. Choi, K. Zhu, J. M. Luther, M. C. Beard, *Nat. Commun.* **2015**, *6*, 7961.
- [40] D. S. Chemla, D. A. B. Miller, P. W. Smith, A. C. Gossard, W. Wiegmann, *IEEE J. Quantum Electron.* **1984**, *20*, 265.
- [41] A. Le Bris, J. F. Guillemoles, *Appl. Phys. Lett.* **2010**, *97*, 113506.
- [42] R. T. Ross, A. J. Nozik, *J. Appl. Phys.* **1982**, *53*, 3813.
- [43] T. Tanaka, A. Harata, T. Sawada, *J. Appl. Phys.* **1997**, *82*, 4033.
- [44] R. K. Ahrenkiel, J. Dashdorj, *J. Vac. Sci. Technol. B* **2004**, *22*, 2063.
- [45] G. J. Rees, *Solid State Electron.* **1985**, *28*, 517.
- [46] D. Kuciauskas, A. Kanevce, P. Dippo, S. Seyedmohammadi, R. Malik, *IEEE J. Photovolt.* **2015**, *5*, 366.
- [47] S. M. Beck, J. E. Wessel, *Appl. Phys. Lett.* **1987**, *50*, 149.
- [48] E. Yablonovitch, D. L. Allara, C. C. Chang, T. Gmitter, T. B. Bright, *Phys. Rev. Lett.* **1986**, *57*, 249.
- [49] G. C. Xing, B. Wu, S. Chen, J. Chua, N. Yantara, S. Mhaisalkar, N. Mathews, T. C. Sum, *Small* **2015**, *11*, 3606.
- [50] G. Xing, N. Mathews, S. Sun, S. S. Lim, Y. M. Lam, M. Graetzel, S. Mhaisalkar, T. C. Sum, *Science* **2013**, *342*, 344.
- [51] M. I. Saidaminov, A. L. Abdelhady, B. Murali, E. Alarousu, V. M. Burlakov, W. Peng, I. Dursun, L. F. Wang, Y. He, G. Maculan, A. Goriely, T. Wu, O. F. Mohammed, O. M. Bakr, *Nat. Commun.* **2015**, *6*, 7586.
- [52] D. Shi, V. Adinolfi, R. Comin, M. J. Yuan, E. Alarousu, A. Buin, Y. Chen, S. Hoogland, A. Rothenberger, K. Katsiev, Y. Losovyj, X. Zhang, P. A. Dowben, O. F. Mohammed, E. H. Sargent, O. M. Bakr, *Science* **2015**, *347*, 519.
- [53] S. D. Stranks, G. E. Eperon, G. Grancini, C. Menelaou, M. J. P. Alcocer, T. Leijtens, L. M. Herz, A. Petrozza, H. J. Snaith, *Science* **2013**, *342*, 341.
- [54] M. A. Green, K. Emery, Y. Hishikawa, W. Warta, *Prog. Photovoltaics* **2011**, *19*, 84.
- [55] C. J. Keavney, V. E. Haven, S. M. Vernon, in *IEEE Conference on Photovoltaic Specialists*, Vol. 1 (Eds: J. D. Meakin), IEEE, Piscataway, NJ, USA, **1990**, p. 141.
- [56] A. B. Sproul, *J. Appl. Phys.* **1994**, *76*, 2851.
- [57] G. Xing, M. H. Kumar, W. K. Chong, X. Liu, Y. Cai, H. Ding, M. Asta, M. Grätzel, S. Mhaisalkar, N. Mathews, T. C. Sum, *Adv. Mater.* **2016**, *28*, 8191.
- [58] A. Wang, J. Zhao, M. A. Green, *Appl. Phys. Lett.* **1990**, *57*, 602.
- [59] J. S. Huang, Y. C. Shao, Q. F. Dong, *J. Phys. Chem. Lett.* **2015**, *6*, 3218.
- [60] K. Vandewal, K. Tvingstedt, A. Gadisa, O. Inganas, J. V. Manca, *Nat. Mater.* **2009**, *8*, 904.
- [61] M. A. Green, *Solid State Electron.* **1981**, *24*, 788.